

Kagome qubit ice

Alejandro Lopez-Bezanilla¹, Jack Raymond², Kelly Boothby²,
Juan Carrasquilla^{3,4}, Cristiano Nisoli^{1,*} and Andrew D. King^{2†}

¹*Theoretical Division, Los Alamos National Laboratory,*

Los Alamos, New Mexico 87545, USA

²*D-Wave Systems, Burnaby, British Columbia, Canada, V5G 4M9, Canada*

³*Vector Institute, University of Toronto,*

Toronto, Ontario, M5G 1M1, Canada and

⁴*Department of Physics and Astronomy,*

University of Waterloo, Waterloo, Ontario, N2L 3G1, Canada

(Dated: January 6, 2023)

Abstract

Topological phases of spin liquids with constrained disorder can host a kinetics of fractionalized excitations. However, spin-liquid phases with distinct kinetic regimes have proven difficult to observe experimentally. Here we present a realization of kagome spin ice in the superconducting qubits of a quantum annealer, and use it to demonstrate a field-induced kinetic crossover between spin-liquid phases. Employing fine control over local magnetic fields, we show evidence of both the Ice-I phase and an unconventional field-induced Ice-II phase. In the latter, a charge-ordered yet spin-disordered topological phase, the kinetics proceeds via pair creation and annihilation of strongly correlated, charge conserving, fractionalized excitations. As these kinetic regimes have resisted characterization in other artificial spin ice realizations, our results demonstrate the utility of quantum-driven kinetics in advancing the study of topological phases of spin liquids.

INTRODUCTION

Dynamics in crystals typically proceeds via motion of topological defects such as dislocation gliding [1]. One might expect the kinetics of disordered systems to be naturally free. But in spin liquids, where disorder is present but constrained, kinetics often also proceeds through defects or excitations are endowed with a conserved topological charge [2]. For instance, frustrated spin systems, such as pyrochlore [3, 4] or square [5–7] spin ices, remain disordered at low temperature, leading to a Pauling residual entropy, and their disorder is constrained by the so-called ice rule [8]. There, kinetics consists of creation/annihilation and walks of localized violations of the ice rule, in the form of emergent magnetic monopoles [9] that conserve a topological charge.

Among spin ices, the kagome ice model [10–18] has been widely studied because it mimics a remarkable variety of natural and artificial systems, from rare-earth pyrochlores [3], to nanomagnetic fabrications [19], gravitationally trapped colloids [15], and many other systems [20–28]. Kagome spin ice can in principle manifest various unusual phases [13–15], but the large energy scales of artificial implementations pose an experimental challenge; thorough measurements of these phases and the physical conditions driving the phase-to-phase transition are scarce.

Here we present a kagome qubit ice realized in a superconducting quantum annealer. Using this experimental platform, we study its field-induced spin-liquid phases and quantum-activated kinetics. We experimentally establish that topological constraints affecting the dynamics proceeds via charge-conserving fractionalized excitations. Using thousands of programmable external magnetic fields, we detune the system from its more common ice-rule-obeying “Ice-I” phase into a field-induced “Ice-II” phase, which exhibits charge order while remaining spin-disordered.

RESULTS

Kagome spin ice

Kagome spin ice consists of magnetic dipoles as classical binary Ising spins arranged along the edges of a hexagonal lattice and therefore on the sites of a kagome lattice. They point from one triangular “ice vertex” (kagome plaquette) to another (Fig. 1a). We can

thus introduce the notion of a magnetic charge for a vertex, defined as the number of spins pointing toward the vertex minus those pointing away from it. Because of the odd coordination, a vertex can host only nonzero, odd charges $q = -3, -1, 1, 3$ (Fig. 1b).

The simplest magnetic kagome model includes interactions only among spins impinging on the same vertex. Since not all pairs of spins at a vertex can simultaneously assume an energy-minimizing head-to-tail configuration, the system is *frustrated*. The ground state is therefore an extensively degenerate ensemble of disordered spins obeying the (pseudo-) ice rule: frustration is minimized when each vertex has two spins pointing in and one pointing out, or vice-versa. This *ice manifold* is often called the *Ice-I phase*, and can be thought as a spin liquid forming an overall neutral plasma of disordered ± 1 magnetic charges. In the *Ice-II phase* [13, 14, 29], disordered spins still obey the ice rule but charges are ordered in an ionic lattice [30–33].

Kagome qubit ice

In this work, we realize kagome spin ice in a quantum annealer. Its superconducting flux qubits are described by the transverse field Ising Hamiltonian

$$H_Q = -\Gamma \sum_i \hat{\sigma}_i^x + \mathcal{J} \left(\sum_i h_i \hat{\sigma}_i^z + \sum_{ij} J_{ij} \hat{\sigma}_i^z \hat{\sigma}_j^z \right), \quad (1)$$

where $\hat{\sigma}^x$ and $\hat{\sigma}^z$ are Pauli matrices on the qubits, \mathcal{J} is an energy prefactor on the classical Ising Hamiltonian, h_i are per-qubit programmable longitudinal fields [?], and J_{ij} are programmable two-qubit couplers. Γ is a transverse field entangling the Pauli matrices and thus controls quantum fluctuations.

Kagome spin ice can be mapped to a classical Ising model [34], and therefore to the Hamiltonian of Eq. (1). Consider alternating A and B vertices pointing up (Δ) and down (∇) respectively in Fig. 1a. We assign an Ising spin value $s_i = +1$ if it points into the A vertex, and $s_i = -1$ if it points into the B vertex (Fig. 1b). (Compare with the Then, standard kagome ice corresponds to the Hamiltonian

$$H_I = J \sum_{\langle i,j \rangle} s_i s_j + \sum_i h_i s_i \quad (2)$$

where each nearest-neighbor spin is coupled antiferromagnetically.

We then embed the kagome lattice in the graph of available two-body couplers, as shown in Fig. 1c, by modifying an embedding of a \mathbb{Z}_2 lattice gauge theory into the transverse-field Ising model [35]. Each kagome site is represented by a ferromagnetic three-qubit chain, and nearest-neighbor chains are coupled antiferromagnetically with two physical couplers. (Three qubits are needed for each kagome lattice site because it is not possible to directly couple two arbitrarily-chosen qubits.) We use h and J (with no index) to denote the total field on a three-qubit chain and the total coupling between two neighboring chains, respectively, obtaining the kagome qubit ice (KQI) Hamiltonian

$$H_{KQI} = -\tilde{\Gamma} \sum_i \tilde{\sigma}_i^x + \mathcal{J} \left(h \sum_i \tilde{\sigma}_i^z + J \sum_{\langle i,j \rangle} \tilde{\sigma}_i^z \tilde{\sigma}_j^z \right), \quad (3)$$

where $\tilde{\Gamma} = \Gamma^3/J_{FM}^2$ is an effective transverse field on the three-qubit chains for a ferromagnetic chain coupling J_{FM} [36], $\tilde{\sigma}_i$ denotes a logical moment represented by a three-qubit chain, and indices i and j are also over three-qubit chains, rather than individual qubits.

Phases

When $\Gamma = \tilde{\Gamma} = 0$ and $h = 0$, the extensively degenerate ground state manifold of H_{KQI} corresponds to that of H_I , which is the commonly seen Ice-I phase [19]. But we can go beyond this regime. In nanoscopic realizations, another phase of lower entropy is possible [30, 31, 33, 37]. In such systems, it is driven by the long range nature of the dipolar interactions [13, 14]. It still has disordered ice-rule obeying spins, but with charges ordered in an ionic lattice where A and B vertices have opposite charge. While the spins remain disordered, though at lower entropy [13, 14, 38], their disorder is topologically constrained: it can be mapped to a dimer cover model [12, 38] and considered a case of *classical topological order* [2, 29, 39, 40]. This is often called the *Ice-II* phase, and its topological nature should show a topologically protected kinetics. (Note also that Ice-II can also be considered a broken symmetry phase with unsaturated order parameter in the context of magnetic fragmentation [18, 41, 42].)

Indeed, the kinetics in the Ice-I phase is *not gapped*: It is possible to flip a single spin—or indeed an extensive number of single spins—without violating the ice rule and thus without creating an excitation (see also Supplementary Informations). Thus, the system can kinetically explore the phase *from within* the local low energy manifold.

Instead, in the Ice-II phase any individual spin flip disrupts the charge balance, thus

creating an excitation. Therefore [2] the kinetics of the Ice-II phase must proceed either via pair creation, motion, and annihilation of gapped excitations, or else via cooperative, ungapped flips of entire loops of head-to-tail spins which do not alter the charge distribution. Such kinetics was never probed in previous realizations of kagome ice because the Ice-II phase has proved very hard to reach [30, 31, 33, 37] (see Supplementary Informations). Fortunately, the quantum annealer offers another route: we can induce it by the field h , acting on σ^z , and then we can study field-induced Ice-II kinetics.

If we define a staggered charge q_s on a vertex such that $q_s = -q$ for A vertices and $q_s = q$ for B vertices, then the field h determines the vertex energies $\varepsilon_{-3}, \varepsilon_{-1}, \varepsilon_{+1}, \varepsilon_{+3}$ for vertices with $q_s = -3, -1, 1, \text{ and } 3$ respectively, as shown in Fig. 2 (see also SI).

For $0 < h/J < 4$, ε_{+1} has the lowest energy, leading to the charge-ordered, spin-disordered Ice-II phase as the ground state. Within this window, Fig. 2 shows a regime crossover at $h/J = 2$. The lowest excitations are charge-order violations upsetting the ionic crystals of charges when $0 < h/J < 2$, and ice rule violations when $2 < h/J < 4$. The two types of excitations are degenerate at $h/J = 2$ where the excitation gap is highest.

Then, for $h/J > 4$, the ground state degeneracy vanishes, replaced by an ordered state in which all A and B vertices have charge -3 and 3 , respectively.

To estimate pseudo-equilibrium properties of the kagome qubit ice in these different phases, we begin with a random spin state and repeatedly expose the system to quantum fluctuations as described by Eq. (1), by cycling the transverse field Γ on and off. An appropriate magnitude of transverse field drives the kinetics of this kagome qubit ice without erasing the state memory, as previously demonstrated in square ice [7]. After each exposure, we read out a classical spin state. This leads to a sequence of states amenable to statistics (see SI).

Fig. 3 summarizes experimental results for varying h/J . Fig. 3a shows real-space samples, represented as vertex charges, for increasing values of h . At $h = 0$ we see the expected disordered charge plasma of the Ice-I phase. Increasing h first leads to ionic ordering of the charge (the Ice-II phase) eventually giving way to a polarized state in which the longitudinal field overcomes the ice rule, forming ionic crystals of ± 3 charge, and all spins have value $s_i = 1$.

Fig. 3b shows the corresponding result in reciprocal space via the Fourier transform of the spins defined as $S(\mathbf{q}) \propto \sum_{ij} e^{i\mathbf{q}(\mathbf{r}_i - \mathbf{r}_j)} (\langle s_i s_j \rangle - \langle s_i \rangle \langle s_j \rangle)$. Our sign convention for the spins

leads to the appearance of peaks only in the Ice-II phase and its proximity, and the formation of pinch points in the topologically protected region with $h/J = 2.5$. In Fig. 3c, cuts of the Fourier transforms through the high-symmetry points in the extended Brillouin zone clearly show growing peaks at K in the proximity of the Ice-II phase. These peaks correspond to the expected logarithmic divergence of the dipolar correlations [12] (see also Fig. 5 in ref [12], obtained from a dimer model). They, and the pinch points, follow therefore from the topological properties induced on the phase by the charge ordering. From an implementation point of view, $S(\mathbf{q})$ reveals a highly symmetric system in which the multi-qubit embedding of kagome spins preserves isotropy. This is an important advance over previous work [7].

Fig. 3d plots the *charge order parameter*, defined as one third the average staggered charge of a vertex. The two broad plateaus at $\pm 1/3$ correspond to the Ice-II phases.

Fig. 3e confirms the high ice-rule obedience throughout the Ice-I and Ice-II phases, which breaks down at $h/J > |4|$ where, from Fig. 2, the lowest energy vertex no longer obeys the ice rule.

Topologically protected quasi-classical kinetics

These measurements validate the annealer’s effectiveness as an experimental platform for probing phases of the Ising kagome spin ice system near a low-temperature thermal equilibrium. Because consecutive output states are separated dynamically by a relatively short exposure to a relatively weak transverse field Γ (compared to J), we can also probe the quasi-classical kinetics.

As mentioned above, in the Ice-II ground state a single spin flip always corresponds to fractionalized excitations, as either violations of the Ice-II charge-order constraint, or violations of the kagome ice rule (Fig. 2). We can define a topological charge (or t-charge) as $q_t = q + 1$, $q_t = q - 1$ for A and B vertices respectively. In the Ice-II charge-ordered ground state, the topological charge is zero on all vertices. Instead, excitations of the Ice-II phase are topologically charged. Their t-charge is conserved: flipping a spin creates a pair of fractional excitations of t-charges ± 2 and zero net t-charge. Further flips can separate the t-charges, which can then annihilated when meeting other, opposite ones. This situation of paired fractional excitations is very reminiscent of square and pyrochlore ice [7, 43], although here the topological charge is not the magnetic charge.

To probe the thermal and quantum-activated kinetics of the Ice-I and Ice-II phases, we compare QA output samples. Between consecutive samples, the qubits are exposed to the a transverse field for $1\ \mu\text{s}$, and at the same time \mathcal{J} is dropped. This protocol is depicted in Fig. 4a. Since the system is in a thermal bath at 12 mK, this allows both quantum and thermal fluctuations to drive dynamics [7].

In agreement with the description above, our results show a kinetics of fractionalized excitations, that can be created and annihilated in pairs of opposite topological charge, and more rarely a kinetics consisting of flips of entire loops of spins—which can always be construed mathematically as creations followed by annihilation of topologically charged pairs.

Fig. 4b shows two representative samples from each of $h/J = 0.5, 2.5, 4$, corresponding roughly to the boundaries and the middle of the field-induced Ice-II phase. Ice-rule and charge-order violations are shown as triangles. Between the two samples, we highlight the spins that flip during the exposure to fluctuations, as well as the motion of fractional excitations.

At $h/J = 0.5$ the charge order is fragile and we are close to the Ice-I phase. We see many excitations popping up erratically, and they are charge order violations, due to their small energy cost (Fig. 2).

At $h/J = 2.5$ we see far fewer excitations, and the kinetics consists of their wandering. We also see flipping of closed loops of spins. One fractional excitation escapes off the boundary, one appears from the boundary, and one moves to another location through a chain of flipped spins. This picture is consistent with the large energy gap shown in Fig. 2, which suppresses pair creation of excitations.

At $h/J = 4$, we again see a regime in which excitations can appear at low cost; these cheap excitations are now ice-rule violations, in contrast to the charge-order violations seen near the Ice-I phase, consistent with the energetics (see Fig. 2).

To quantify the creation/annihilation and motion of fractional excitations, we consider the subgraph of the honeycomb lattice whose edges correspond to flipped spins (Fig. 4c–d) between consecutive states. We measure the degrees (valencies) of honeycomb sites in this graph. A closed loop of flipped spins results in only degree-two honeycomb sites. Conversely, an open chain of flipped spins will have degree two in the interior, and degree one on the ends. This can involve the motion of a fractional excitation, with or without

creation/annihilation. In general, degree-two spins correspond to motion of excitations, while degree-one spins correspond to creation/annihilation.

Fig. 4e shows that the system is overall most active around $h/J = 0$ and $h/J = 4$, which corresponds to points of degeneracy (see Fig. 2) where excitations are cheapest. The plot of the relative frequency of excitation motion over pair creation/annihilation shows a maximum around $h/J = 2$, the point of maximum gap: where excitations are most expensive, kinetics consists mostly of their random walk, much like monopoles in square or pyrochlore spin ice.

The non-monotonicity of the curves in Fig. 3e shows that in kagome qubit ice, by tuning the gap of the phase, the topological protection of the kinetics can be controlled, from a hard to distinguish soup of excitations at $h/J = 0, 4$, to a clear picture of creation/annihilation and motion of fractionalized excitations around the value $h/J = 2$.

DISCUSSION

We have realized kagome qubit spin ice in 2742 superconducting flux qubits of a quantum annealing processor and explored its field-induced spin-liquid ice phases. We have studied the quantum-activated, topologically protected kinetics of the Ice-II phase and shown that it proceeds via creation/annihilation and propagation of charge-conserving fractionalized excitations. We emphasize that quantum fluctuations are used here only to drive kinetics, but can be employed in the future to study entangled states. Furthermore, the kagome antiferromagnet in a transverse field Γ has a rich ground-state phase diagram [44] arising from high-order perturbations in Γ , which may be probed in future work. Our results demonstrate that quantum annealers are capable of implementing exotic programmable phases of frustrated spin sliquids, whose gap and topologically-protected kinetic regimes can be finely tuned.

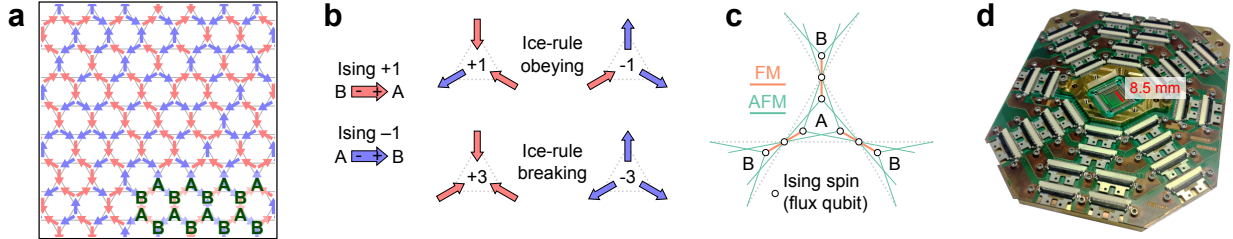


FIG. 1: **Kagome qubit ice.** **A**, Kagome spin ice consists of magnetic dipoles on the edges of a hexagonal lattice, which point in or out of triangular plaquettes (vertices) of the dual kagome lattice (gray lines). **B**, Each vertex in a given configuration has a nonzero charge: ± 1 -charged vertices satisfy the kagome ice rule; ± 3 -charged vertices do not. Denoting triangles pointing up and down by A and B respectively, one can map dipoles to Ising spins according to whether not the dipole points into an A triangle. **C**, In the kagome qubit ice, each kagome site is realized using a ferromagnetically-coupled three-qubit chain. Sites impinging on the same triangular ice vertex are coupled antiferromagnetically, leading to geometric frustration. **D**, Optical image of the superconducting quantum annealing processor in a sample holder. 2742 qubits are used to realize a 913-spin kagome ice.

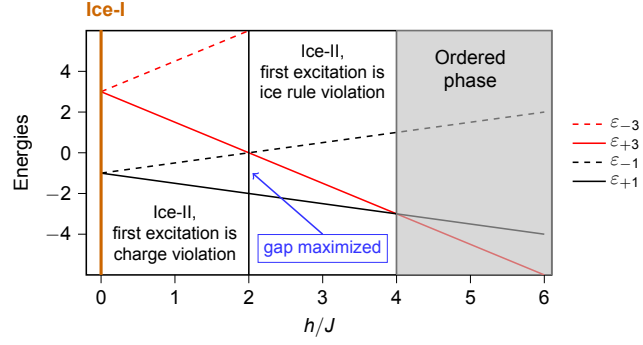


FIG. 2: **Ice vertex energies** (normalized to J). In the Ice-I phase ($h = 0$), the ice-rule vertex states ε_{+1} and ε_{-1} are degenerate. Detuning h leads energetic preference towards the (staggered) +1-charged configurations. Within the ice region $0 \leq h/J \leq 4$, the energy gap is maximized at $h/J = 2$, where charge-imbalance excitations are degenerate with ice-rule excitations.

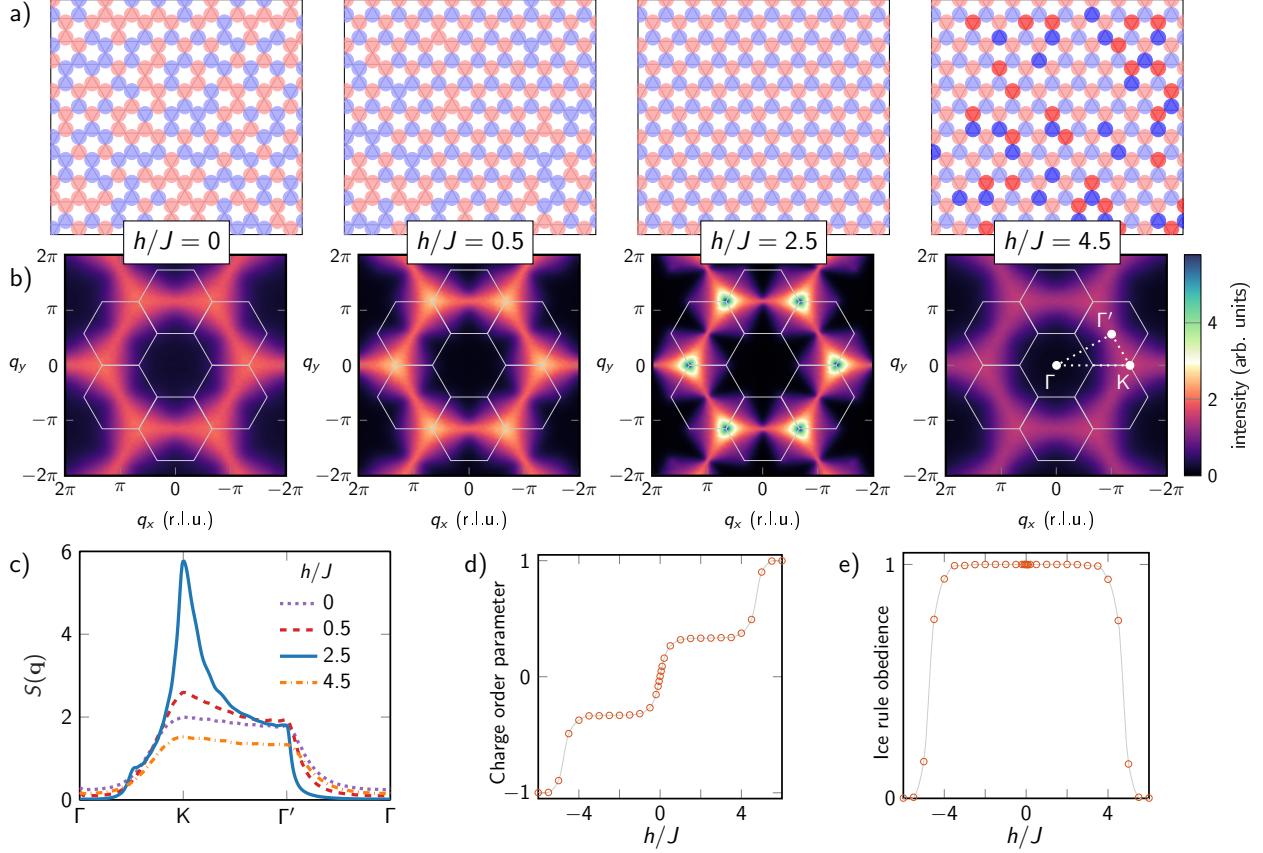


FIG. 3: Field-induced charge phases and qubit ice structure. **A**, Charge states for varying external field h . At $h = 0$, vertices have no energetic preference between -1 and $+1$ charge (light blue and red respectively), leading to charge disorder. As h increases, A and B vertices energetically favor -1 and $+1$ charge respectively, leading to long-range order in the staggered charge. Eventually h polarizes the sites, leading to a preponderance of -3 and $+3$ charged vertices (dark blue and red respectively). **B**, Fourier transforms $S(\mathbf{q})$ calculated from QA experimental output, with Brillouin zone in gray. **C**, Cuts of $S(\mathbf{q})$ for varying h/J through high-symmetry points Γ , K , and Γ' (shown in **b**) show the effect of the longitudinal field on peak height at K and pinch-point width at Γ' . **D**, Charge order parameter. **E**, Proportion of vertices obeying the ice rule.

FIG. 4: **Kinetics and field-induced topological protection.** **A**, Within the quantum annealer, the kinetics is driven by a reverse anneal protocol wherein the qubits (Eq. (1)) are exposed to quantum fluctuations (Γ) and thermal fluctuations (T/\mathcal{J}) for a duration of $1\ \mu\text{s}$ between projected classical output states. **B**, Quantum annealer output samples. For each h/J , two consecutive states are shown, along with the spin-flip difference between them. For the states, up and down triangles denote charge-order violations and ice-rule violations respectively. For the spin-flip differences, crosses denote excitations in state i , and circles denote excitations in state $i + 1$. For $h/J = 2.5$, near the middle of the field-induced Ice-II phase, the two excitation types are nearly degenerate, with a large gap. Thus excitations are suppressed although they can move freely. **C–D**, Flipped spins (**c**) form a subgraph of the dual honeycomb lattice (**D**), and the degree distribution in this subgraph relates to quasiparticle behavior; $d = 2$ sites correspond with closed loops or long chains of flipped spins, indicating collective spin flips or motion of fractional excitations. **E**, Field-dependence of the degree distribution indicates different field-induced kinetic regimes.

-
- * cristiano@lanl.gov; These two authors contributed equally
- † aking@dwavesys.com; These two authors contributed equally
- [1] D. R. Nelson, *Defects and geometry in condensed matter physics* (Cambridge University Press, 2002).
- [2] C. L. Henley, *Journal of Physics: Condensed Matter* **23**, 164212 (2011).
- [3] K. Matsuhira, Z. Hiroi, T. Tayama, S. Takagi, and T. Sakakibara, *Journal of Physics: Condensed Matter* **14**, L559 (2002), ISSN 0953-8984.
- [4] S. T. Bramwell and M. J. Harris, *Journal of Physics Condensed Matter* **32** (2020).
- [5] Y. Perrin, B. Canals, and N. Rougemaille, *Nature* **540**, 410 (2016).
- [6] A. Farhan, M. Saccone, C. F. Petersen, S. Dhuey, R. V. Chopdekar, Y. L. Huang, N. Kent, Z. Chen, M. J. Alava, T. Lippert, et al., *Science Advances* **5**, 1 (2019).
- [7] A. D. King, C. Nisoli, E. D. Dahl, G. Poulin-Lamarre, and A. Lopez-Bezanilla, *Science* **373**, 576 (2021).
- [8] L. Pauling, *Journal of the American Chemical Society* **57**, 2680 (1935), ISSN 0002-7863.
- [9] C. Castelnovo, R. Moessner, and S. L. Sondhi, *Nature* **451**, 42 (2008).
- [10] B. Sriram Shastry and B. Sutherland, *Physica B+C* **108**, 1069 (1981), ISSN 03784363.
- [11] A. Wills, R. Ballou, and C. Lacroix, *Physical Review B* **66**, 144407 (2002).
- [12] R. Moessner and S. L. Sondhi, *Physical Review B* **68**, 064411 (2003).
- [13] G. Möller and R. Moessner, *Phys. Rev. B* **80**, 140409 (2009).
- [14] G.-W. Chern, P. Mellado, and O. Tchernyshyov, *Phys. Rev. Lett.* **106**, 207202 (2011).
- [15] A. Libál, C. Nisoli, C. J. O. Reichhardt, and C. Reichhardt, *Phys. Rev. Lett.* **120**, 027204 (2018), URL <https://link.aps.org/doi/10.1103/PhysRevLett.120.027204>.
- [16] L. Balents, *Nature* **464**, 199 (2010).
- [17] V. Raban, C. Suen, L. Berthier, and P. Holdsworth, *Physical Review B* **99**, 224425 (2019).
- [18] E. Lhotel, L. D. Jaubert, and P. C. Holdsworth, *Journal of Low Temperature Physics* **201**, 710 (2020).
- [19] Y. Qi, T. Brintlinger, and J. Cumings, *Physical Review B* **77**, 1 (2008).
- [20] A. Libál, C. J. O. Reichhardt, and C. Reichhardt, *Phys. Rev. Lett.* **102**, 237004 (2009).
- [21] Y.-L. Wang, X. Ma, J. Xu, Z.-L. Xiao, A. Snezhko, R. Divan, L. E. Ocola, J. E. Pearson,

- B. Janko, and W.-K. Kwok, *Nature Nanotechnology* **13**, 560 (2018), ISSN 1748-3387.
- [22] C. Xue, J.-Y. Ge, A. He, V. S. Zharinov, V. V. Moshchalkov, Y. H. Zhou, A. V. Silhanek, and J. Van de Vondel, *Phys. Rev. B* **97**, 134506 (2018).
- [23] P. Mellado, A. Concha, and L. Mahadevan, *Physical Review Letters* **109**, 257203 (2012).
- [24] A. Duzgun and C. Nisoli, *Phys. Rev. Lett.* **126**, 047801 (2021).
- [25] K. Zhao, H. Deng, H. Chen, K. A. Ross, V. Petříček, G. Günther, M. Russina, V. Hutanu, and P. Gegenwart, *Science* **367**, 1218 (2020).
- [26] M. Hua, B. Xia, M. Wang, E. Li, J. Liu, T. Wu, Y. Wang, R. Li, H. Ding, J. Hu, et al., *The Journal of Physical Chemistry Letters* **12**, 3733 (2021), ISSN 1948-7185.
- [27] A. S. Meeussen, E. C. Oğuz, Y. Shokef, and M. van Hecke, *Nature Physics* **16**, 307 (2020), ISSN 1745-2473.
- [28] B. Pisanty, E. C. Oguz, C. Nisoli, and Y. Shokef, *SciPost Phys.* **10**, 136 (2021).
- [29] A. J. Macdonald, P. C. W. Holdsworth, and R. G. Melko, *Journal of Physics: Condensed Matter* **23**, 164208 (2011), ISSN 0953-8984.
- [30] S. Zhang, I. Gilbert, C. Nisoli, G. W. Chern, M. J. Erickson, L. O'Brien, C. Leighton, P. E. Lammert, V. H. Crespi, and P. Schiffer, *Nature* **500**, 553 (2013), ISSN 00280836.
- [31] J. Drisko, S. Daunheimer, and J. Cumings, *Physical Review B* **91**, 224406 (2015).
- [32] D. Levis, L. F. Cugliandolo, L. Foini, and M. Tarzia, *Physical review letters* **110**, 207206 (2013).
- [33] L. Anghinolfi, H. Luetkens, J. Perron, M. Flokstra, O. Sendetskyi, A. Suter, T. Prokscha, P. Derlet, S. Lee, and L. Heyderman, *Nature communications* **6** (2015).
- [34] S. Zhang, J. Li, I. Gilbert, J. Bartell, M. J. Erickson, Y. Pan, P. E. Lammert, C. Nisoli, K. Kohli, R. Misra, et al., *Physical review letters* **109**, 087201 (2012).
- [35] C. Chamon, D. Green, and Z.-C. Yang, *Physical Review Letters* **125**, 067203 (2020), ISSN 0031-9007.
- [36] A. D. King, C. D. Batista, J. Raymond, T. Lanting, I. Ozfidan, G. Poulin-Lamarre, H. Zhang, and M. H. Amin, *PRX Quantum* **2**, 030317 (2021).
- [37] N. Rougemaille, F. Montaigne, B. Canals, A. Duluard, D. Lacour, M. Hehn, R. Belkhou, O. Fruchart, S. El Moussaoui, A. Bendouan, et al., *Phys. Rev. Lett.* **106**, 057209 (2011).
- [38] P. E. Lammert, X. Ke, J. Li, C. Nisoli, D. M. Garand, V. H. Crespi, and P. Schiffer, *Nat. Phys.* **6**, 786 (2010).

- [39] R. Z. Lamberty, S. Papanikolaou, and C. L. Henley, *Physical review letters* **111**, 245701 (2013).
- [40] Y. Lao, F. Caravelli, M. Sheikh, J. Sklenar, D. Gardeazabal, J. D. Watts, A. M. Albrecht, A. Scholl, K. Dahmen, C. Nisoli, et al., *Nature Physics* **14**, 723 (2018).
- [41] B. Canals, I.-A. Chioar, V.-D. Nguyen, M. Hehn, D. Lacour, F. Montaigne, A. Locatelli, T. O. Montes, B. S. Burgos, and N. Rougemaille, *Nature Communications* **7**, 11446 (2016), ISSN 2041-1723.
- [42] M. Brooks-Bartlett, S. T. Banks, L. D. Jaubert, A. Harman-Clarke, and P. C. Holdsworth, *Physical Review X* **4**, 011007 (2014).
- [43] C. Castellano and C. Chamon, *Physical Review B* **76**, 174416 (2007).
- [44] R. Moessner, S. L. Sondhi, and P. Chandra, *Physical Review Letters* **84**, 4457 (2000), ISSN 0031-9007.
- [45] K. Boothby, C. Enderud, T. Lanting, R. Molavi, N. Tsai, M. H. Volkmann, F. Altomare, M. H. Amin, M. Babcock, A. J. Berkley, et al., *Architectural considerations in the design of a third-generation superconducting quantum annealing processor* (2021), 2108.02322.
- [46] A. D. King, J. Carrasquilla, J. Raymond, I. Ozfidan, E. Andriyash, A. J. Berkley, M. Reis, T. Lanting, R. Harris, F. Altomare, et al., *Nature* **560**, 456 (2018).
- [47] K. Boothby, P. Bunyk, J. Raymond, and A. Roy, *Next-Generation Topology of D-Wave Quantum Processors* (2020), 2003.00133, URL <http://arxiv.org/abs/2003.00133>.

Acknowledgments

The authors acknowledge the contributions of technical staff at D-Wave, without whom this work would not be possible. The work of ALB and CN was carried out under the auspices of the U.S. DoE through the Los Alamos National Laboratory, operated by Triad National Security, LLC (Contract No. 892333218NCA000001). JC acknowledges support from the Natural Sciences and Engineering Research Council (NSERC), the Shared Hierarchical Academic Research Computing Network (SHARCNET), Compute Canada, Google Quantum Research Award, and the Canadian Institute for Advanced Research (CIFAR) AI chair program. Resources used in preparing this research were provided, in part, by the Province of Ontario, the Government of Canada through CIFAR, and companies sponsoring the Vector Institute.

Competing interests

The authors declare no competing interests.

Author Contributions

J.C. first proposed the idea of a Kagome embedding in a D-Wave QA to A.D.K.. A.D.K., A.L.-B., C.N., and J.C. conceived the project. C.N., A.D.K. contributed to the design of the experiments. A.D.K. and K.B. realized the embedding. J.R. performed supporting measurements. A.D.K., A.L.-B. performed QA experiments. A.D.K. performed data analysis. C.N. provided the theoretical framework for experiment design and result interpretation. C.N. drafted the manuscript with A.D.K. All authors contributed to the final version of the manuscript.

Methods

The QA processor used in this work was a D-Wave Advantage QPU (Fig. 1d) housed in Burnaby, BC, Canada, operating at $T = 12$ mK and accessed remotely. The QPU contains 5627 operable superconducting flux qubits of which we used 2739 to implement our kagome qubit spin ice. The architecture is discussed in Ref. [45].

In quantum annealing, the Hamiltonian (1) in the Main Text is controlled by an annealing parameter s ranging from 0 to 1:

$$H_Q(s) = -\Gamma(s) \sum_i \sigma_i^x + \mathcal{J}(s) \left(\sum_i h_i \sigma_i^z + \sum_{ij} J_{ij} \sigma_i^z \sigma_j^z \right), \quad (4)$$

where $\Gamma(0) \gg \mathcal{J}(0)$ and $\Gamma(1) \approx 0 \ll \mathcal{J}(1)$.

Thus a typical “forward anneal”, in which s is ramped linearly for the duration of anneal time t_a ($s = t/t_a$) begins in an easily-prepared superposition ground state and ends in a low-energy state of a classical Ising Hamiltonian. For simulating spin systems, it has proven useful [7, 46] to employ a “quantum evolution Monte Carlo” method, in which a chain of classical samples S_0, \dots, S_k is generated. To generate S_i , the system is initialized in state S_0 at the end of the anneal ($s = 1$), then “reverse annealed” back to some intermediate s^* , paused at s^* to allow equilibration for some time t_p , then quickly quenched back to

$s = 1$. Although this method can be used to estimate observables from a transverse field Ising model at s^* [46], here we just use quantum fluctuations as a driver of mixing dynamics between low energy state in the kagome ice system.

In this work we generate chains of $k = 128$ samples, starting with a random initial state S_0 . To estimate equilibrium properties (Fig. 3) we use $t_p = 256 \mu\text{s}$ and discard the first 64 samples of each chain (and the random initial state) as Monte Carlo burn-in. For dynamics inquiries (Fig. 4) we use $t_p = 1 \mu\text{s}$. In both cases we interrogate Hamiltonian (4) using $s^* = 0.32$, which was chosen to give an appropriate amount of mixing in one microsecond (smaller s leads to faster mixing since both Γ/\mathcal{J} and T/\mathcal{J} are larger [7]). When statistical quantities are estimated, we take the average of 200 repeated experimental iterations; each iteration includes a call to the QPU for each value of h probed.

Graph embedding

The qubits in the QA processor are intercoupled in a ‘‘Pegasus’’ layout [47], in which a qubit is coupled to up to 15 other qubits. From these available couplers we select a geometry that represents a kagome graph using three qubits per kagome spin as depicted in Fig. 1c. We show the full embedded lattice in Fig. 6. The kagome embedding does not require the use of all qubits, and it is possible to embed a defect-free lattice with no site vacancies, despite the existence of some inoperable qubits (empty circle in Fig. 6c).

Since ferromagnetic chains are sometimes broken, they are majority-voted to provide an unambiguous mapping from the qubit system to the kagome system. We run all experiments presented herein with $J_{ij} = 0.9$ for AFM couplers and $J_{ij} = -1.5$ for FM couplers. This choice of ferromagnetic coupling is sufficient to guarantee that chains are almost never broken in QPU output, despite the frustration in the system.

Disorder suppression

In this application we perform many experiments on a single programmed lattice, whose classical ground state is highly degenerate. Under such conditions it is appropriate to refine the general-purpose QA calibration by exploiting symmetries in the system.

For example, when $h = 0$ each qubit should have average magnetization $\langle s_i \rangle = 0$. Thus we

tune per-qubit flux offsets to balance qubits at zero for $h = 0$, then use the same flux offsets when $h \neq 0$. In this experiment, we are not interested in probing boundary conditions. Rather, we want to simulate the thermodynamic limit of an infinite system. In an infinite system, for any fixed h , the correlation of two neighboring kagome sites $\langle s_i s_j \rangle$ is the same. Thus we fine-tune the AFM couplers to promote this property. Since the three-qubit FM chains are almost never broken, we do not fine-tune the FM couplers. Similarly, for any fixed $h \neq 0$, the magnetization of each qubit should be equal; we fine-tune the per-qubit fields h_i to promote this property (maintaining the property that the average $\frac{1}{N} \sum_i h_i$ does not change from the nominal value h). These calibration refinements are performed before collecting the analyzed data. Fig. 7 shows an example of this refinement for $J = 0.9$, $h = 0.6$, with the magnetizations and correlations achieved, and the programmed values that achieve them.

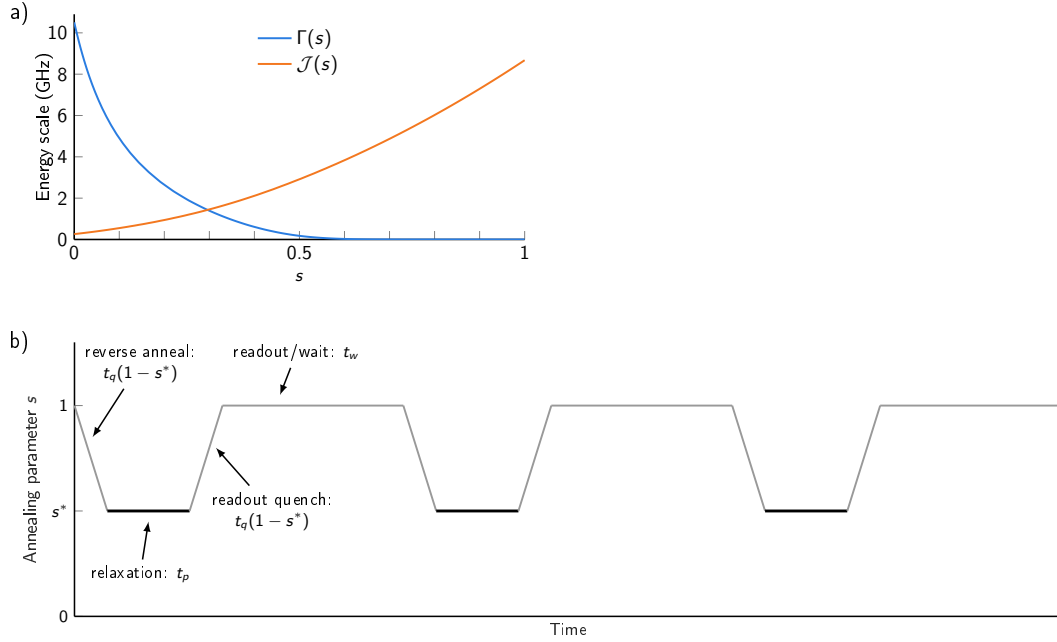


FIG. 5: **Quantum annealing schedule and protocol.** **a**, Transverse field $\Gamma(s)$ and Ising energy scale $\mathcal{J}(s)$ as a function of annealing parameter s . Note that the total coupling between two three-qubit chains is $1.8\mathcal{J}$. **b**, Quantum evolution Monte Carlo method. A sequence of classical readout states is generated by repeated exposure to quantum fluctuations and thermal fluctuations.

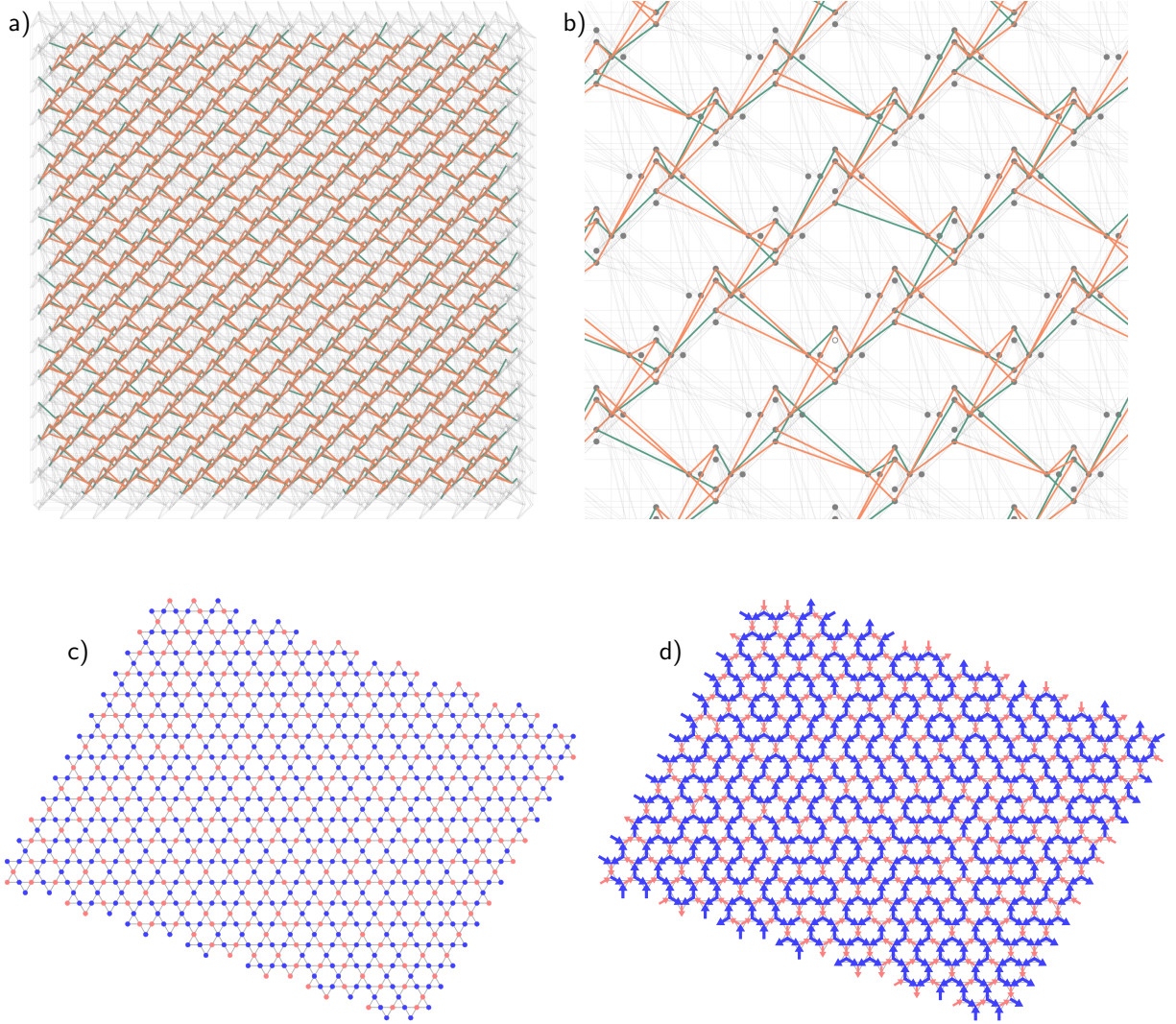


FIG. 6: **Embedding of the kagome lattice into the qubit graph.** **a–b**, Each kagome site is represented by three qubits, coupled together ferromagnetically in a chain ($J_{ij} = -1.5$). The entire qubit graph and embedding are shown in **a** with green and orange lines representing FM and AFM couplers respectively; **b** shows a detailed zoom, with operable and inoperable qubits represented by filled and empty circles respectively. **c–d**, The embedding shown in **a** realizes a 729-site kagome lattice, which can be viewed as Ising spins (**c**), or magnetic dipoles (**d**).

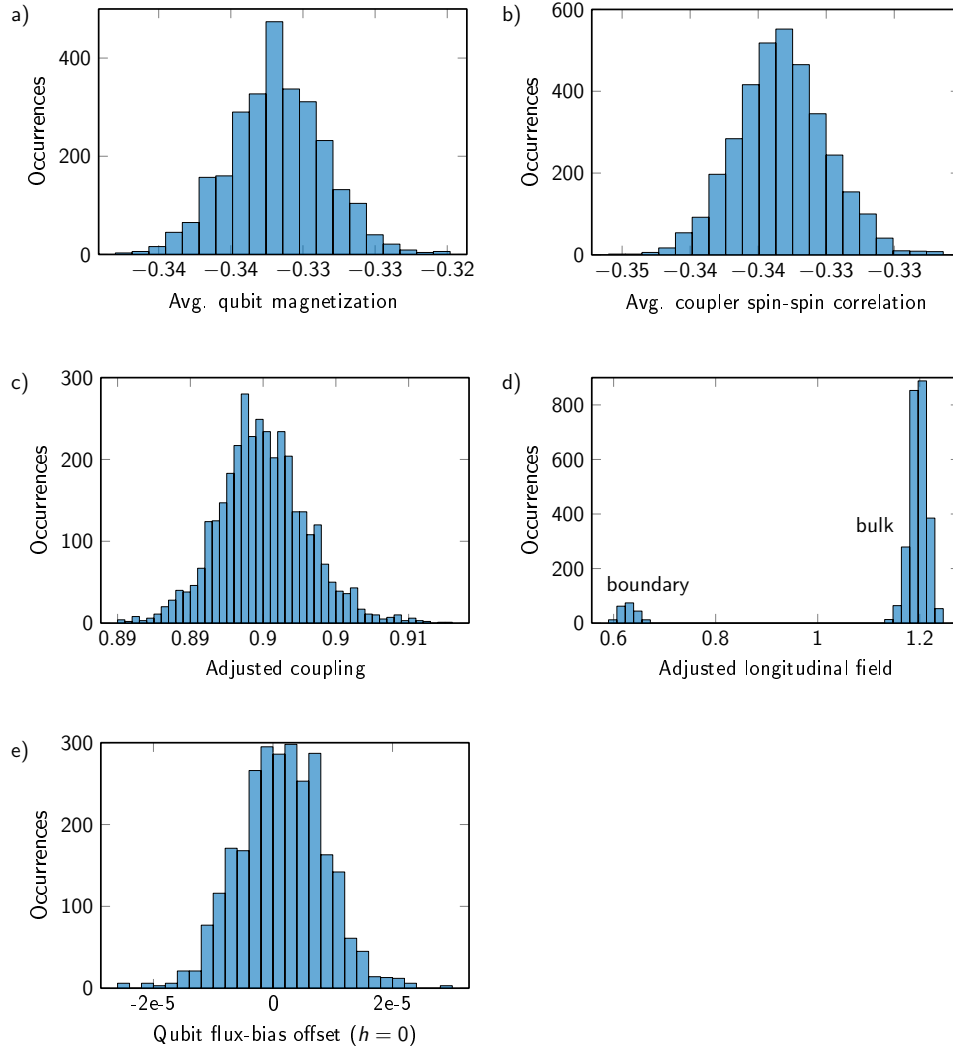


FIG. 7: **Suppressed disorder with fine-tuned Hamiltonian terms.** Example data are shown for nominal AFM coupling values of $J = 0.9$ and local fields of $h = 0.6$. **a–b**, Over 100 iterations, tightly-concentrated average qubit magnetizations and spin-spin correlations of coupled pairs indicate a balanced degenerate ice system. **c–e**, This is achieved by small adjustments of couplers (**c**), adjustment of fields (**d**), and qubits are balanced using flux-bias offsets at $h = 0$ that are also used at nonzero h . Note the two modes in **d**, where boundary spins are assigned roughly half the field of bulk spins, in accordance with their degree in the graph, to achieve similar magnetizations.